Journal of Hazardous Materials 219–220 (2012) 26–34

Contents lists available at SciVerse ScienceDirect

Journal of Hazardous Materials

journal homepage: www.elsevier.com/locate/jhazmat

Room temperature synthesis and highly enhanced visible light photocatalytic activity of porous BiOI/BiOCl composites nanoplates microflowers

Fan Dong[a,*], Yanjuan Sun[a], Min Fu[a], Zhongbiao Wu[b], S.C. Lee[c]

[a] College of Environmental and Biological Engineering, Key laboratory of Catalysis Science and Technology of Chongqing Education Commission, Chongqing Technology and Business University, Chongqing 400067, China
[b] Department of Environmental Engineering, Zhejiang University, Hangzhou 310027, China
[c] Department of Civil and Structural Engineering, Research Center for Environmental Technology and Management, The Hong Kong Polytechnic University, Hong Kong, China

ARTICLE INFO

Article history:
Received 19 December 2011
Received in revised form 5 March 2012
Accepted 6 March 2012
Available online 14 March 2012

Keywords:
BiOI/BiOCl composites
Visible light
Photocatalytic activity
Nitric oxide
Template free

ABSTRACT

This research represents a highly enhanced visible light photocatalytic removal of 450 ppb level of nitric oxide (NO) in air by utilizing flower-like hierarchical porous BiOI/BiOCl composites synthesized by a room temperature template free method for the first time. The facile synthesis method avoids high temperature treatment, use of organic precursors and production of undesirable organic byproducts during synthesis process. The result indicated that the as-prepared BiOI/BiOCl composites samples were solid solution and were self-assembled hierarchically with single-crystal nanoplates. The aggregation of the self-assembled nanoplates resulted in the formation of 3D hierarchical porous architecture containing trimodel mesopores. The coupling to BiOI with BiOCl led to down-lowered valence band (VB) and up-lifted conduction band (CB) in contrast to BiOI, making the composites suitable for visible light excitation. The BiOI/BiOCl composites samples exhibited highly enhanced visible light photocatalytic activity for removal of NO in air due to the large surface areas and pore volume, hierarchical structure and modified band structure, exceeding that of P25, BiOI, C-doped TiO_2 and Bi_2WO_6. This research results could provide a cost-effective approach for the synthesis of porous hierarchical materials and enhancement of photocatalyst performance for environmental and energetic applications owing to its low cost and easy scaling up.

1. Introduction

The synthesis of hierarchical porous materials assembled from nanoscale building blocks, especially three-dimensional (3D) hierarchical architectures that are assembled by two-dimensional (2D) nanoplates or nanosheets, have received intensive research interest [1–3]. Due to the well-defined hierarchical porous structure, they could offer opportunities to explore their novel or enhanced properties, such as adsorption, sensing, energy conversion, catalysis, pollution control [4–6]. Various routes have been employed to synthesize 3D hierarchical porous architectures, including template and template free methods [7–9]. Template method usually requires tedious preparation procedures of template modification, precursor attachment and core removal, which would lead to the cost increase and further limit the potential applications [7]. The capability of template method is also limited by the availability of types of templates. Therefore, it is highly desirable to explore of facile and cost-effective approach for the synthesis of 3D hierarchical porous materials. The template free method is one of the most promising routes due to its advantages of low cost, environmental friendly, mild synthesis condition, and potential large-scale application [8,9]. It is especially ideal if the template free method can be conducted at room temperature, which could further reduce the production cost in the synthesis. A variety of hierarchical or hollow materials with improved properties have been successfully prepared using room temperature template free synthesis method in the past few years, such as TiO_2, MnO_2, Cu_2S, $CdMoO_4$, $ZnSn(OH)_6$ and so on [10–14].

Semiconductor photocatalysis driven by visible light has become the world hot topic of intensive interest due to its potential applications in environmental purification and solar energy conversion by utilizing visible light in solar or indoor light source [15–18]. Recently, hierarchical BOX (X = Cl, Br, I) nanoplates architectures with photocatalytic activities have been synthesized by sol–gel, hydrothermal/solvothermal, precipitation, reverse microemulsions, and ionic-assisted methods [19–25]. The internal structure of $(BiO)_2^{2+}$ layers interleaved by double slabs of X^- atoms guided the growth of BiOX at certain axis to form 2D nanoplate morphology. Some results proved that 2D nanostructures favored the transfer of electrons and holes generated inside the crystal

* Corresponding author. Tel.: +86 23 62769785 605; fax: +86 23 62769785 605.
E-mail address: dfctbu@126.com (F. Dong).

0304-3894/$ – see front matter © 2012 Elsevier B.V. All rights reserved.
doi:10.1016/j.jhazmat.2012.03.015

surface and promoted the electrons/holes separation, which was advantageous to improve the photocatalytic activity [26–28]. In order to further improve the visible light activity of BOX based photocatalytic materials for application, composite semiconductor systems have been developed by applying the principle of band gap engineering, such as BiOCl/WO_3, BiOCl/$NaBiO_3$, BiOCl/BiOBr, BiOBr/BiOI, BiOI/AgI, BiOI/TiO_2, BiOI/BiOCl [29–35]. These composites materials exhibited enhanced visible light photocatalytic activities in degradation of various pollutants.

In the present study, flower-like hierarchical porous BiOI/BiOCl composites self-assembled with nanoplates were synthesized from inorganic precursors by a room temperature template free method. Although hierarchical BiOI/BiOCl composites with enhanced photocatalytic performance have been synthesized by hydrothermal method, the preparation conditions require relative high temperature and use of organic solvent. Besides, undesirable organic byproducts would be produced, which is not environmentally friendly [35]. Our facile method here avoids high temperature treatment, use of organic precursors and production of undesirable organic byproducts in the synthesis. As expected, the as-prepared BiOI/BiOCl composites exhibited highly enhanced visible light photocatalytic activity for the removal of 450 ppb level of nitric oxide (NO) in air, outstanding several good photocatalysts including P25, BiOI, C-doped TiO_2 and Bi_2WO_6. The structural features of the BiOI/BiOCl composites were characterized in detail and a new mechanism for the activity enhancement was proposed.

2. Experimental

2.1. Chemicals and synthesis of BiOI/BiOCl composites

All chemicals used in this study were analytical grade (Sigma–Aldrich) and were used without further purification. Distilled water was used in all experiments. BiOI/BiOCl composites were synthesized by a template free method at room temperature (25 °C). In a typical synthesis, stoichiometric amounts of KCl and KI were dissolved in 150 mL of H_2O. 0.02 mol of $Bi(NO_3)_3{\cdot}5H_2O$ was added into the above solution slowly. The mixtures were adjusted to pH of 10 by using 1 M of $NH_3{\cdot}H_2O$ solution and stirred vigorously for 12 h. After the stirring was completed, the resulting solid product was collected by filtration, washed several times with deionized water and then dried at 60 °C to get the final sample. Depending on the molar ratio of KI to KCl (1:0, 0.75:0.25, 0.5:0.5, 0.25:0.75 and 0:1), different BiOI/BiOCl composites can be synthesized and labeled as BOI, $BOI_{0.75}Cl_{0.25}$, $BOI_{0.5}Cl_{0.5}$ $BOI_{0.25}Cl_{0.75}$, and BOCl, respectively. It was known that the hydrolysis of $Bi(NO_3)_3$ in water produced the $BiONO_3$ [36]. The formation of BiOI/BiOCl composites from the starting compounds follows the Eqs. (1)–(4).

$$NH_3{\cdot}H_2O \rightarrow NH_4^+ + OH^- \quad (1)$$

$$Bi(NO_3)_3 + H_2O \rightarrow BiONO_3 + 2H^+ + 2NO_3^- \quad (2)$$

$$H^+ + OH^- \rightarrow H_2O \quad (3)$$

$$BiONO_3 + xI^- + (1-x)Cl^- \rightarrow BiOI_xCl_{1-x} + NO_3^- \quad (4)$$

For reference, C-doped TiO_2 and Bi_2WO_6 were also prepared according to our previous methods [37,38].

2.2. Characterization instruments

The crystal phases of the sample were analyzed by X-ray diffraction with Cu Kα radiation (XRD: model D/max RA, Rigaku Co., Japan). A scanning electron microscope (SEM, JEOL model JSM-6490, Japan) was used to characterize the morphology of the obtained products. The morphology and structure of the samples were examined by transmission electron microscopy (TEM: JEM-2010, Japan). Nitrogen adsorption–desorption isotherms were obtained on a nitrogen adsorption apparatus (ASAP 2020, USA). All the samples were degassed at 200 °C prior to measurements. X-ray photoelectron spectroscopy with Al Kα X-rays ($h\nu$ = 1486.6 eV) radiation operated at 150 W (XPS: Thermo ESCALAB 250, USA) was used to investigate the surface properties and to probe the total density of the state (DOS) distribution in the valence band (VB). The shift of the binding energy due to relative surface charging was corrected using the C1s level at 284.8 eV as an internal standard. The UV–vis diffuse reflection spectra were obtained for the dry-pressed disk samples using a Scan UV–VIS spectrophotometer (UV–VIS DRS: UV-2450, Shimadzu, Japan) equipped with an integrating sphere assembly, using $BaSO_4$ as reflectance sample. The spectra were recorded at room temperature in air ranged from 250 to 800 nm.

2.3. Photocatalytic experiments

The photocatalytic activity was investigated by removal of NO at ppb levels in a continuous flow reactor at ambient temperature. The volume of the rectangular reactor, made of stainless steel and covered with Saint-Glass, was 4.5 L (30 cm × 15 cm × 10 cm). A 300 W commercial tungsten halogen lamp (General Electric) was vertically placed outside the reactor. Four mini-fans were used to cool the flow system. For the visible light photocatalytic activity test, UV cutoff filter (400 nm) was adopted to remove UV light in the light beam. For photocatalytic activity test under simulated solar light, the UV cutoff filter was removed. Appropriate of photocatalyst (0.15 g) was dispersed in 30 mL water and sonochemically treated for 30 min. The resulted suspension was transferred to a dish with a diameter of 12.0 cm. The coated dish was then pretreated at 70 °C to remove water in the suspension and the solid photocatalyst was finally coated on the dish uniformly. The NO gas was acquired from a compressed gas cylinder at a concentration of 100 ppm of NO (N_2 balance, BOC gas) with traceable National Institute of Standards and Technology (NIST) standard. The initial concentration of NO was diluted to about 450 ppb by the air stream supplied by a zero air generator (Thermo Environmental Inc., model 111). The desired relative humidity (RH) level of the NO flow was controlled at 70% by passing the zero air streams through a humidification chamber. The gas streams were premixed completely by a gas blender, and the flow rate was controlled at 3.3 L/min by a mass flow controller. After the adsorption–desorption equilibrium was achieved, the lamp was turned on. The concentration of NO was continuously measured by a chemiluminescence NO analyzer (Thermo Environmental Instruments Inc., model 42c), which monitors NO, NO_2, and NO_x (NO_x represents NO + NO_2) with a sampling rate of 0.7 L/min. The removal ratio (η) of NO was calculated as η (%) = $(1 - C/C_0) \times 100\%$, where C and C_0 are concentrations of NO in the outlet stream and the feeding stream, respectively. The kinetics of photocatalytic NO removal reaction is a pseudo first order reaction at low NO concentration as $\ln(C_0/C) = kt$, where k is the initial apparent rate constant.

3. Results and discussion

3.1. Phase structure

Fig. 1 shows the XRD patterns of the as-prepared BiOI/BiOCl samples. The XRD patterns for BiOI and BiOCl can be indexed to tetragonal phase BiOI (JCPDS card no. 73-2062) and tetragonal phase BiOCl (JCPDS card no. 06-0249), respectively. With the variation of Cl molar ratio from 0 to 1.0, all diffraction peaks gradually shift to higher angles (i.e., a smaller spacing between the diffraction planes), which can be ascribed to the fact that Cl^- ion has a smaller

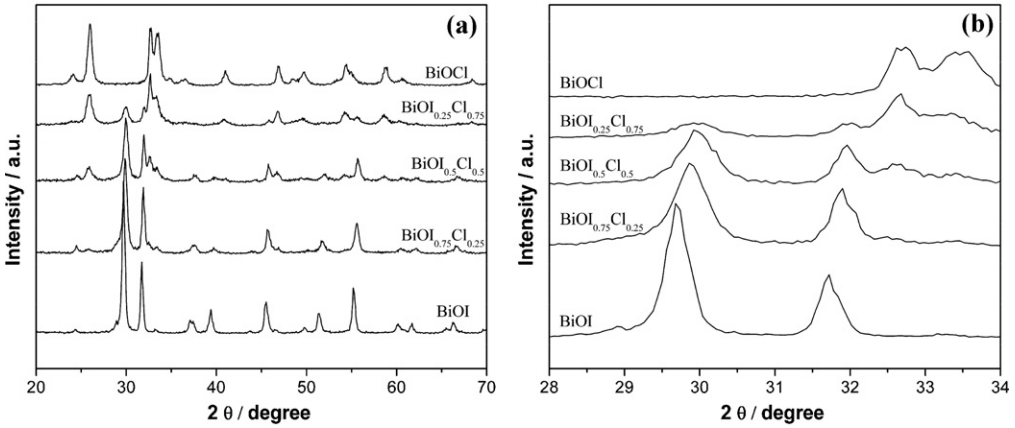

Fig. 1. XRD patterns of the as-prepared BiOI/BiOCl samples (a) and enlarged view of the diffraction region between 28 and 34° (b).

ionic radius than does I^- ion (1.81 vs. 2.20). The enlarged image of Fig. 1 illustrates the change of some strongest peaks clearly. The regular gradual shift of the XRD patterns as function of the Cl^- ion molar ratio reveals that the as-prepared BiOI/BiOCl composites are a group of solid solutions [31,39].

Fig. 2 shows the Raman spectra of BiOCl, $BiOCl_{0.75}I_{0.25}$ and BiOI samples. The BiOX with a space group of $D_{4h}{}^7$, has two molecular formulas per unit cell with the Raman active modes of A_{1g}, B_{1g}, and E_g [40]. Pure BiOCl shows two distinctive bands and one weak band. The strong band at 144 cm^{-1} (assigned to the A_{1g} internal Bi—Cl stretching mode) and the band at 197 cm^{-1} (assigned to the E_g internal B—Cl stretching mode) can be observed. The E_g external Bi—Cl stretching is probably overlapped by the strong band at 144 cm^{-1}. The week band at 396 cm^{-1} can be ascribed to E_g and B_{1g} band, produced by motion of the oxygen atoms [40]. For pure BiOI, the band at 148 cm^{-1} is assigned to the E_g internal B—I stretching mode. After coupling the two components, most of the bands for BiOCl and BiOI vanished and only the band of BiOCl at 144 cm^{-1} with low intensity was preserved. A new broadened band at 156 cm^{-1} appeared. The reduction of original bands of BiOCl and BiOI and the generation of new band further confirmed the formation of solid solution [31].

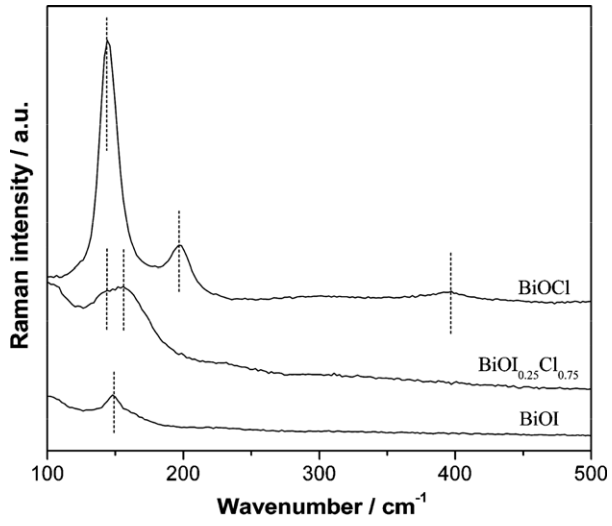

Fig. 2. Raman spectra of BiOCl, $BiOCl_{0.75}I_{0.25}$ and BiOI samples.

3.2. Morphological structure

The surface morphology of the as-prepared samples was examined by SEM, as shown in Fig. 3a–f. It can be seen that all the samples are in the form of microflowers, which are assembled hierarchically by many nanoplates. The microflowers for different samples have slightly different morphology. The formation of 2D nanoplate structure can be ascribed to the internal structure of BiOX, where $(BiO)_2{}^{2+}$ layers sandwiched by two slabs of X^- atoms, leading to the anisotropic growth of BiOX at certain axis to form 2D nanoplates [20,31]. Driven by the minimization of the total energy of the system, these primary nanoplates tend to form 3D hierarchical flower-like microspheres by self-assembly in the growth process without the assistant of templates as sphericity has the minimal surface energy. With the nanoplates self-assembled hierarchical structure, light can be reflected within the interconnected nanoplates multiplely, which could enhance light-harvesting ability of the materials [28,41,42].

The morphological structure of $BiOI_{0.25}Cl_{0.75}$ sample was further examined by TEM and HRTEM, as shown in Fig. 4. The TEM image in Fig. 4a further shows that $BiOI_{0.25}Cl_{0.75}$ sample is irregular flower-like architectures, consistent with the SEM observation. TEM images taken from the edge of the individual microstructure in Fig. 4b and c reveal that the as-prepared material is highly crystallized and self-assembled with nanoplates. The nanoplates are very thin (about 15 nm) and transparent to the electron beam. An HRTEM image of a single nanoplate in the architecture is shown in Fig. 4d. The *d* values of lattice spacing are measured to be 0.338 and 0.301 nm, matching with the spacing of the (1 0 1) crystal plane of BiOCl and (0 1 2) crystal plane of BiOI in BiOI/BiOCl composites. This result indicates the presence of the mixed phase of BiOI and BiOCl in $BiOI_{0.25}Cl_{0.75}$ sample, consistent with XRD result. The inset of SAED pattern in Fig. 4d shows an array of clear and regular diffraction spots of the single nanoplate, which implies that the nanoplate is single-crystalline in nature. Thus, the formation of $BiOI_{0.25}Cl_{0.75}$ hierarchical composites originates from the self-assembly of these single-crystalline nanoplates.

3.3. Specific surface areas and pore structure

The specific BET surface areas (S_{BET}) and pore structure of the prepared samples was investigated using adsorption–desorption measurements. As shown in Table 1, the S_{BET} of the BiOI/BiOCl composites samples gradually increases from 13.67 to 17.40 m^2/g, compared to pure BiOI (5.71 m^2/g) and BiOCl (9.02 m^2/g). The

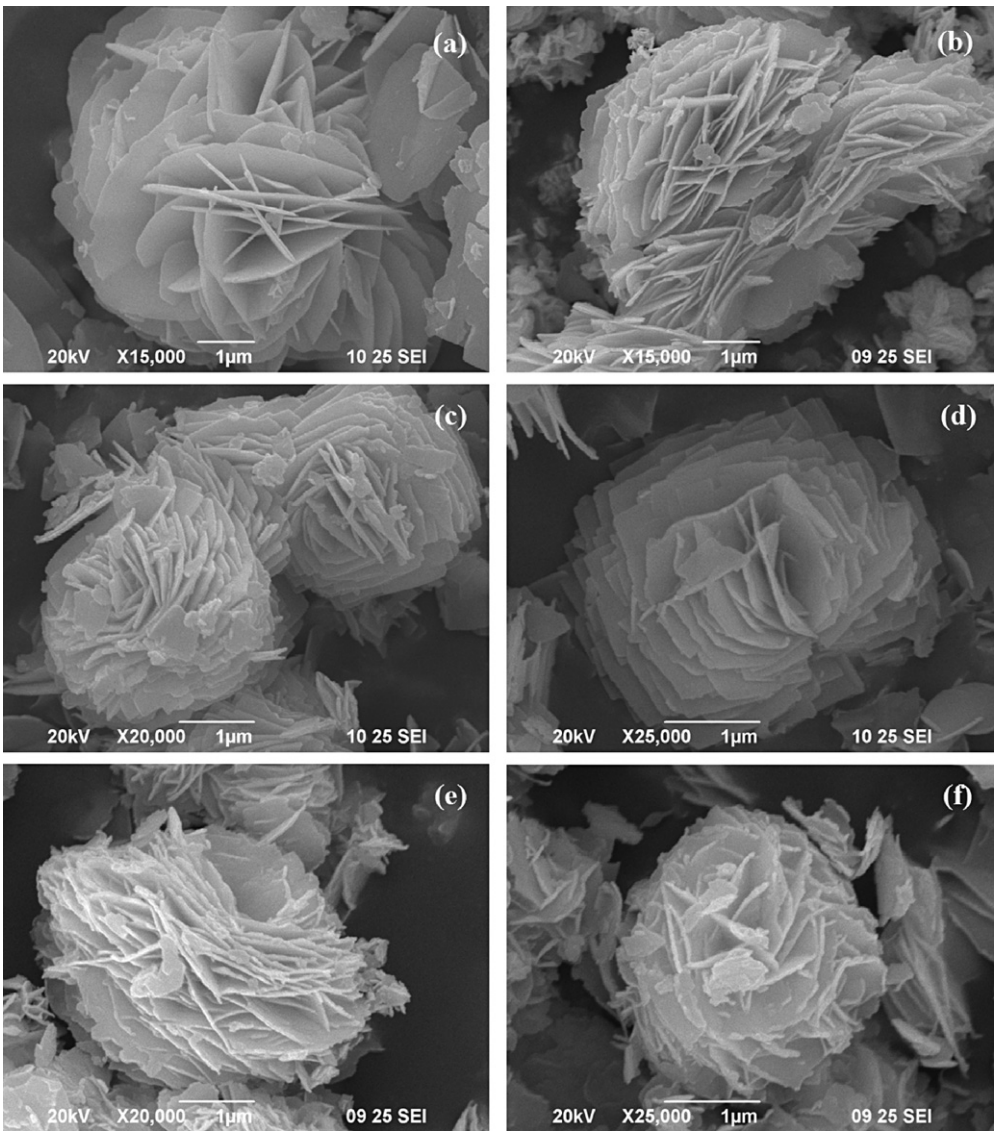

Fig. 3. SEM images of BiOI (a), BiOCl (b), $BiOI_{0.75}Cl_{0.25}$ (c), $BiOI_{0.5}Cl_{0.5}$ (d), and $BiOI_{0.25}Cl_{0.75}$ (e, f).

pore volume of composites samples increases from 0.0754 to 0.0880 cm^3/g, compared to pure BiOI (0.0267 cm^3/g) and BiOCl (0.0484 cm^3/g). The $BiOI_{0.25}Cl_{0.75}$ samples have the maximum S_{BET} and pore volume. A greater specific surface area and pore volume of photocatalysts can supply more surface active sites and make reactants transport easier, leading to an enhancement of the photocatalytic performance [43]. Thus, the large S_{BET} and pore volume of BiOI/BiOCl composites samples may play a role in enhancing the photocatalytic activity.

Fig. 5a shows the nitrogen adsorption–desorption isotherms of the porous samples. According to the Brunauer –Deming–Deming–Teller (BDDT) classification, the majority of physisorption isotherms can be grouped into six types [44]. The isotherms of all the samples are types IV, indicating the pore-size distributions in the mesoporous regions. The shapes of hysteresis loops are of type H3, which is associated with mesopores formed due to aggregation of plates-like particles [44]. This result is consistent with SEM that the aggregation of the self-assembled nanoplates resulted in the formation of 3D hierarchical flower-like architecture.

Fig. 5b shows the corresponding pore-size distribution (PSD) of the samples. As can be seen that for the BiOI sample, the PSD curve

Table 1
Specific BET surface areas, pore parameters, removal ratio and initial reaction constants for the as-prepared and reference samples.

Samples	S_{BET} (m^2/g)	Total volume (cm^3/g)	Peak pore diameter (nm)	η (%)	k (min^{-1})
BiOI	5.71	0.0267	3.7/18.3	14.9	0.047
$BiOI_{0.75}Cl_{0.25}$	13.67	0.0754	2.2/3.8/20.7	42.4	0.14
$BiOI_{0.5}Cl_{0.5}$	16.41	0.0871	2.2/3.8/19.8	44.9	0.14
$BiOI_{0.25}Cl_{0.75}$	17.40	0.0880	2.3/3.8/11.6	54.6	0.20
BiOCl	9.02	0.0484	2.4/3.9/19.3	4.2	0.0091
P25	51.2	0.090	22.0	10.3	0.034
C-doped TiO_2	122.5	0.248	3.5	21.8	0.069
Bi_2WO_6	10	–	20.0	7.9	0.033

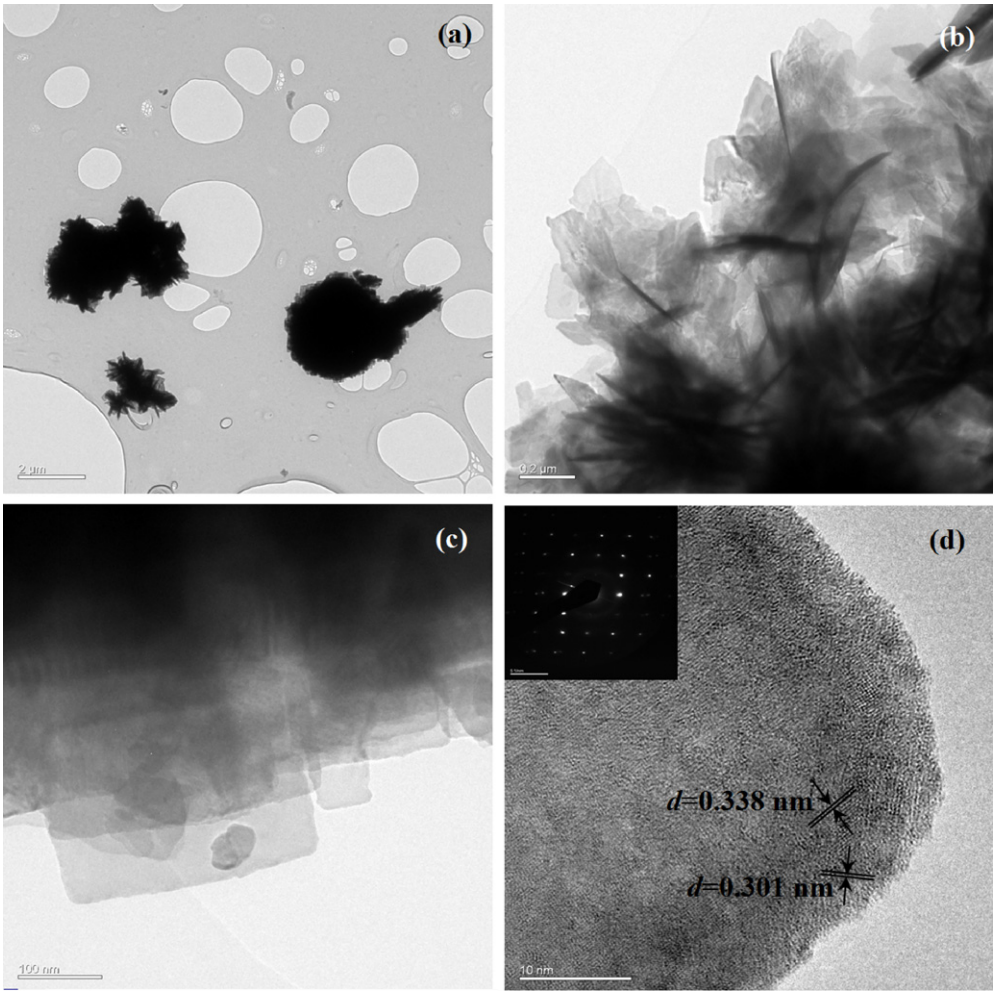

Fig. 4. TEM (a, b, c) and HETEM (d) images of $BiOI_{0.25}Cl_{0.75}$ sample. The inset in (d) shows the SAED of a single nanoplate.

is bimodal with smaller (~3.7 nm) and larger (~18.3 nm) mesopores. For other 4 samples, the PSD curve is tri-modal with smaller (~2.2–2.4 nm), small (~3.8–3.9 nm) and large (~11.6–20.7 nm) mesopores. As the nanoplates do not contain pores (Fig. 4c), the smaller mesopores in the range of 2.0–4.0 nm may reflect porosity within nanoplates. The larger mesopores in the range of 11.0–21.0 nm may be ascribed to the pores formed between stacked nanoplates (Fig. 3). Such self-organized porous architecture might be extremely useful in photocatalysis because they provide efficient transport pathways for reactant and product molecules [28,43]. The S_{BET} and pore parameters of reference samples are summarized in Table 1.

3.4. XPS analysis

To further investigate the surface chemical compositions and valence band states of the as-prepared samples, XPS studies were conducted, and the spectra were illustrated in Fig. 6. It can be seen

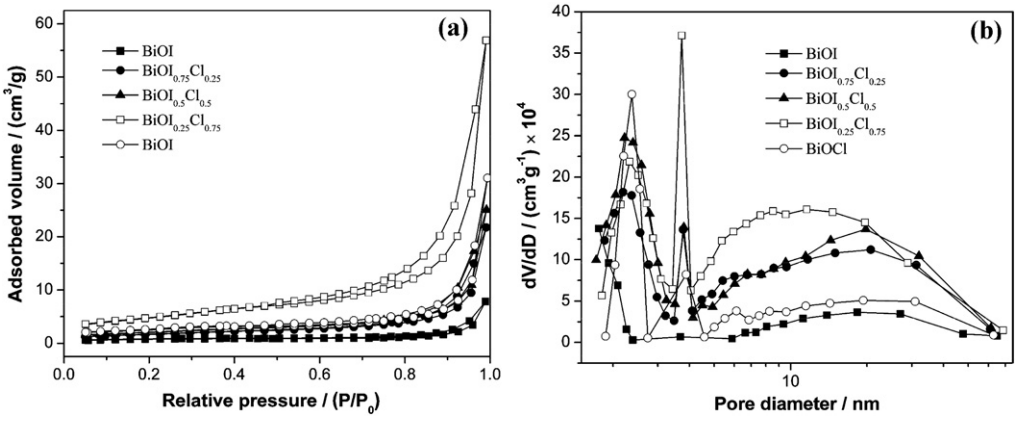

Fig. 5. N_2 adsorption–desorption isotherm (a) and pore-size distribution curves (b) of the BiOI/BiOCl samples.

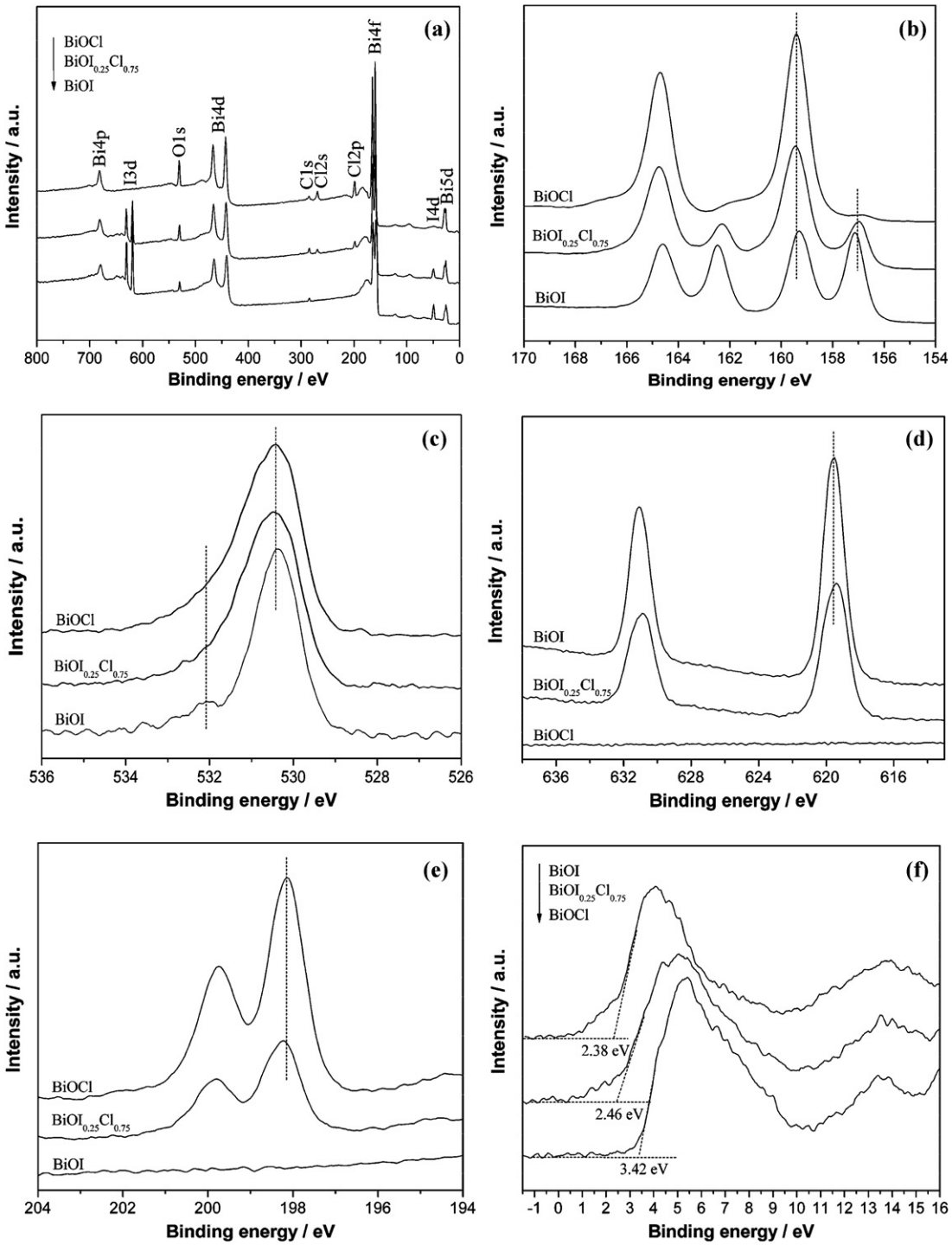

Fig. 6. XPS spectra of BiOI, $BiOI_{0.25}Cl_{0.75}$ and BiOCl samples for survey (a), Bi 4f (b), O 1s (c), I 3d (d), Cl 2p (e) and VB (f).

from the XPS survey spectra (Fig. 6a) that the as-prepared samples contain not only Bi, O, I and Cl elements but also some C. The XPS peak for C 1s (284.8 eV) is ascribed to the adventitious carbon from the XPS instrument.

Typical high-resolution XPS spectra for Bi 4f are shown in Fig. 6b. Two peaks at 159.4 and 164.7 eV for the three samples are assigned to Bi $4f_{7/2}$ and Bi $4f_{5/2}$, respectively, which is characteristic of Bi^{3+} in BiOI, $BiOCl_{0.75}I_{0.25}$ and BiOCl [21]. Besides, two other peaks around 157.0 and 162.3 eV ascribed to Bi $4f_{7/2}$ and Bi $4f_{5/2}$ in Bi^0 can be observed. Because the samples do not contain Bi^0 as confirmed by XRD (Fig. 1), it must be generated in the process of XPS measurement. Considering the band gap of the samples (Fig. 7b), they can be excited by the Al Kα X-rays ($h\nu = 1486.6$ eV) of XPS instrument to produce electrons/hole pairs. The Bi^{3+} can in turn be reduced to Bi^0 by the photogenerated electrons. The content of Bi^0 is highest in BiOI and lowest in BiOCl. This result implies that BiOX is not very stable under strong irradiation.

Fig. 6c shows the high-resolution XPS spectra for the O 1s region, which can be fitted into two peaks. The main peak at 530.4 eV is attributed to the Bi—O bonds in $(BiO)_2^{2+}$ slabs of BiOX layered structure, and the peak at 532.1 eV is assigned to the hydroxyl groups on the surface [21]. As to the high-resolution spectra of the I 3d

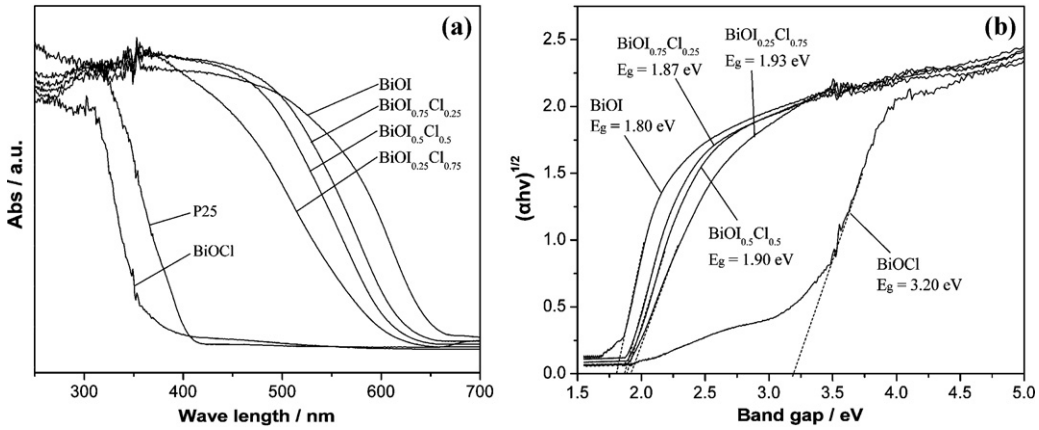

Fig. 7. UV–vis DRS of as-prepared BiOI/BiOCl samples (a) and the plotting of $(\alpha h\nu)^{1/2}$ vs. photon energy (b).

(Fig. 6d), two peaks at 631.0 and 619.4 eV attributed to I $3d_{3/2}$ and I $3d_{5/2}$ respectively, can be ascribed to I^- in BiOI and $BiOI_{0.25}Cl_{0.75}$ samples [34]. The high-resolution XPS spectra of Cl 2p in Fig. 6e show two peaks at 199.8 and 198.2 eV, which can be ascribed to Cl $2d_{1/2}$ and Cl $2p_{3/2}$, respectively [20].

To determine the relative positions of conduction band (CB) and VB edges, the total densities of states of VB were measured, as shown in Fig. 6f. In contrast to BiOI, the $BiOI_{0.25}Cl_{0.75}$ demonstrates a VB maximum down-lowered from 2.38 to 2.46 eV. Compared to BiOCl, the $BiOCl_{0.75}I_{0.25}$ exhibits a VB maximum up-shifted from 3.42 to 2.46 eV. The shift of VB maximum position for $BiOI_{0.25}Cl_{0.75}$ can be attributable to the formation of solid solution, as confirmed by XRD and Raman. Additional electronic states between 0 and 3.0 eV of $BiOI_{0.25}Cl_{0.75}$ resulted from iodine orbital can also be observed in comparison with BiOCl.

3.5. Optical properties

The band gap structure of a semiconductor photocatalyst is an important factor in determining the photocatalytic performance. Fig. 7a shows the UV–vis DRS of as-prepared BiOI/BiOCl samples. It can be seen that pure BiOCl absorbs only UV light with an absorption edge at 370 nm and pure BiOI shows a huge optical absorbance in the visible light region with an absorption edge at 670 nm. The absorption edge of the composites samples shifts monotonically to longer wavelengths as the amount of BiOI increases. The band gap energy can be estimated from the intercept of the tangents to the plots of $(\alpha h\nu)^{1/2}$ vs. photon energy, as shown in Fig. 7b [18,20]. The band gaps of BiOI and BiOCl are determined to be about 1.80 and 3.20 eV, consistent with reported values [20,35]. The band gap of $BiOI_{0.25}Cl_{0.75}$ is 1.93 eV, which is located between the band gap values of BiOI and BiOCl due to solid solution structure. The band gap values of the samples are listed in Table 2.

3.6. Enhanced visible light photocatalytic activity for removal of NO in air

The as-prepared hierarchical porous BiOI/BiOCl samples were used to photocatalytic removal of NO in air phase in order to demonstrate their potential ability for air purification. Fig. 8a shows the variation of NO concentration (C/C_0%) with irradiation time over the samples under visible light irradiation ($\lambda > 420$ nm). Here, C_0 is the initial concentration of NO, and C is the concentration of NO after photocatalytic reaction for time t. As a comparison, photocatalytic oxidation of NO over P25, C-doped TiO_2 and Bi_2WO_6 are also performed under identical conditions. As previously proved, NO could not be photolyzed under light irradiation [21]. In the presence of photocatalytic materials, the NO reacted with the photo-generated reactive radicals and produced HNO_2 and HNO_3, which involved four reactions displayed in Eqs. (5)–(8) [21].

$$NO + 2^{\bullet}OH \rightarrow NO_2 + H_2O \quad (5)$$

$$NO_2 + {}^{\bullet}OH \rightarrow NO_3^- + H^+ \quad (6)$$

$$NO + NO_2 + H_2O \rightarrow 2HNO_2 \quad (7)$$

$$NO + {}^{\bullet}O_2^- \rightarrow NO_3^- \quad (8)$$

As shown in Fig. 8a and Table 1, after 30 min irradiation, BiOCl shows negligible visible light activity due to the large band gap of 3.2 eV. P25 consists of 80% of anatase and 20% of rutile. The band gap of rutile TiO_2 is 3.0 eV and can be excited by visible light with wavelength shorter than 413 nm. P25 exhibits weak visible light activity with a removal rate of 10.3% (k, 0.0091 min^{-1}) due to the existence of small amount of rutile phase in P25. BiOI with a band gap of 1.80 eV can be excited by visible light and exhibits decent removal rate of 14.9% (k, 0.047 min^{-1}). The NO removal rate reaches at 21.8% (k, 0.069 min^{-1}) over C-doped TiO_2 as it is a well known good visible light driven photocatalyst. The widely investigated Bi_2WO_6 photocatalyst also show certain visible light activity of 7.9% (k, 0.034 min^{-1}). Interestingly, by coupling BiOCl and BiOI, the visible light activity over BiOI/BiOCl composites is dramatically enhanced with removal rate over 40%, exceeding all of the reference samples. When the molar ratio of iodine to chloride is 1:3, the activity of BiOI/BiOCl composites ($BiOI_{0.25}Cl_{0.75}$) reaches maximum removal rate of 54.6% (k, 0.20 min^{-1}), 21 times higher than that of BiOCl and 4 times higher than that of BiOI, as shown in Fig. 8b. The optimal $BiOI_{0.25}Cl_{0.75}$ composites were also more efficient than other types of visible light photocatalytic materials for NO removal reported in

Table 2
Absolute electronegativity, calculated CB edge, calculated VB position and band gap energy for BiOI, BiOCl and $BOI_{0.25}Cl_{0.75}$ at the point of zero charge.

Semiconductors	Absolute electronegativity (X) (/eV)	Calculated CB position (eV)	Calculated VB position (eV)	Band gap energy E_g (eV)
BiOI	5.99	0.62	2.42	1.80
$BOI_{0.25}Cl_{0.75}$	6.25	0.56	2.49	1.93
BiOCl	6.34	0.24	3.44	3.20

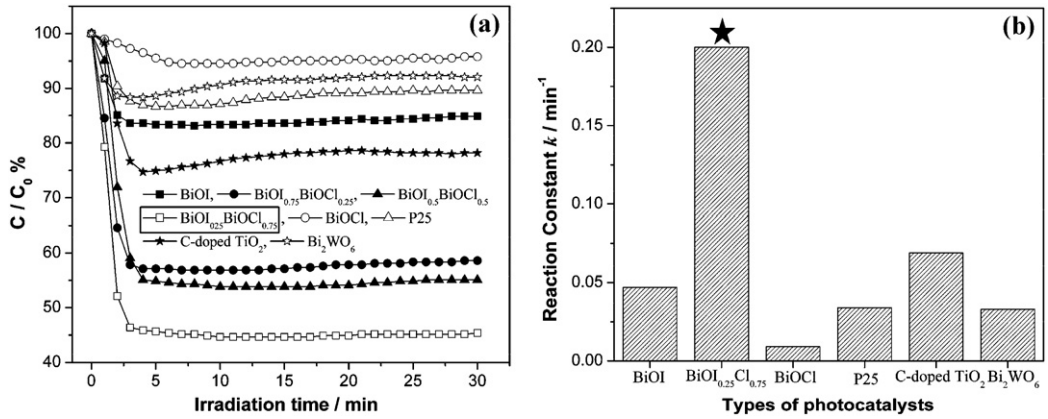

Fig. 8. Photocatalytic activities of the as-prepared BiOI/BiOCl samples under visible light irradiation. P25, C-doped TiO_2 and Bi_2WO_6 were used as reference samples.

literature [17,21,38] including N-doped TiO_2, Bi_2WO_6 and BiOBr, which indicated that the as-prepared BiOI/BiOCl composites were highly efficient visible light driven photocatalysts. Jasra and co-workers showed that the oxidizing radical species given by the Cl^- ions reduced the rate of degradation of Fe metal ion impregnated TiO_2 [45]. The Cl^- ions impregnated photocatalyst was different from BiOI/BiOCl composites intrinsically. For Cl^- ions impregnated photocatalyst, these impregnated free Cl^- ions were on the catalyst surface. The Cl^- ions could take part in the photocatalytic reaction, resulting in reduction the degradation rate. However, there is no free Cl^- and I^- ions on the BiOI/BiOCl composites because the BiOI and BiOCl are well crystallized (Fig. 1). Therefore, Cl^- and I^- ions should have no negative effect on BiOI/BiOCl composites photocatalyst.

The BiOI/BiOCl composites photocatalyst shows little deactivation after 30 min reaction, revealing the superior photocatalytic performance of the BiOI/BiOCl composites sample. The small decrease in activity for some other samples was due to the accumulation of oxidation product (HNO_3) on the catalyst surface [18,21]. For the optimal $BiOI_{0.25}Cl_{0.75}$ composites sample, the NO removal rate can be well maintained after three recycles under visible light, which can be attributed to the hierarchical mesoporous structure and large surface areas. The open mesoporous architecture with large surface area facilitated the molecular transport of reactants and products [21].

3.7. Mechanism of activity enhancement of BiOI/BiOCl composites

Photocatalytic activity of a semiconductor depends on various factors such as surface area, pore volume, morphology, light absorption, band structure and nature of dopant if any.

In order to further investigate the effect of band structure on the activity of the as-prepared samples, the positions of CB edge and VB edge were calculated using a simple theoretical method. The conduction band edge (E_{CB}) of a semiconductor at the point of zero charge (pH_{ZPC}) can be predicted by the equation $E_{CB} = X - E^C - 1/2E_g$ [35], where X is the absolute electronegativity of the semiconductor. E_C is the energy of free electrons on the hydrogen scale (~4.5 eV). E_g is the band gap energy of the semiconductor. The calculated CB and VB edge positions of BiOI, $BiOI_{0.25}Cl_{0.75}$ and BiOCl are listed in the Table 2, which is consistent with experimental result from VB XPS. According to this result, a schematic illustration of the band gap structures for the samples can be drawn and shown in Fig. 9. Pure BiOCl with a large band gap can not be excited by visible light. By coupling BiOCl with BiOI, the $BiOI_{0.25}Cl_{0.75}$ composites have a band gap of 1.93 eV with down-lowered VB and up-lifted CB in contrast to BiOI, which is suitable for visible light excitation. The down-lowering of VB edge position makes the photogenerated

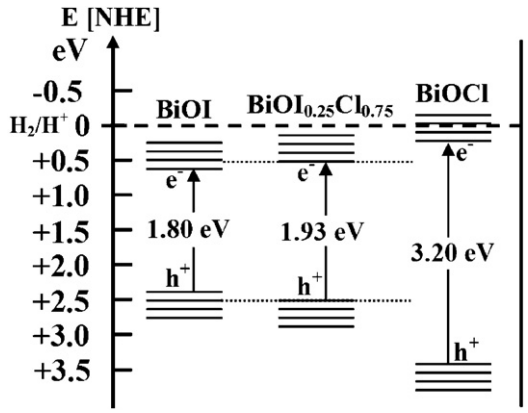

Fig. 9. Schematic illustration of the band gap structures of BiOCl, $BiOCl_{0.75}I_{0.25}$ and BiOI.

holes of $BiOI_{0.25}Cl_{0.75}$ composites have more powerful oxidation ability than that of BiOI [46], which also contributed to the corresponding enhanced visible light photocatalytic activity (Fig. 8). As the content of BiOI in the composites samples further increase from 0.25 to 0.75, the VB edge position would be lowered and the band gap decreased (Fig. 7b), which makes visible light activity decrease. The result also implies that band gap of BiOX can be rationally engineered by coupling selective components.

Judging from Fig. 5 and Table 1, we can find that the hierarchical BiOI/BiOCl composites samples have larger S_{BET} and pore volume than that of pure BiOI and BiOCl. The highly enhanced visible light photocatalytic activity of $BiOI_{0.25}Cl_{0.75}$ sample respect to BiOI, C-doped TiO_2 and Bi_2WO_6 can be ascribed to the synergetic effect of large S_{BET} and pore volume, hierarchical structure and modified band structure with down-lowered VB edge position [28,41–43,46]. The as-prepared BiOI/BiOCl composites photocatalyst could offer an effective material for environmental and energetic applications owing to the low cost and easy scaling up of synthesis method. Our result could also provide new insights into the design of high performance visible light driven photocatalysts and room temperature synthesis of other hierarchical porous materials.

4. Conclusion

Flower-like hierarchical porous BiOI/BiOCl composites were synthesized by a template free method at room temperature. This facile and mild synthesis method is free of using organic precursors and production of undesirable byproducts during synthesis process. A solid solution was formed for the composites samples which

were self-assembled hierarchically by single-crystal nanoplates. The formation of 3D hierarchical porous architecture containing tri-model mesopores can be ascribed to the aggregation of the self-assembled nanoplates. The coupled BiOI/BiOCl samples suitable for visible light excitation had a down-lowered VB and up-lifted CB in contrast to BiOI. The as-prepared BiOI/BiOCl composites samples exhibited highly enhanced visible light photocatalytic activity in removal of NO in air, exceeding that of P25, BiOI, C-doped TiO_2 and Bi_2WO_6. The large surface areas and pore volume, hierarchical structure and modified band structure in all contributed to the dramatic activity enhancement. The research results could not only provide new insights into the room temperature synthesis of hierarchical porous nanomaterials with enhanced properties, but also could provide an effective approach for design of high performance visible light driven photocatalysts for environmental and energetic applications owing to its low cost and easy scaling up.

Acknowledgements

This research is financially supported by the National Natural Science Foundation of China (51108487), the Program for Young Talented Teachers in Universities (Chongqing, 2011), the National High Technology Research and Development Program (863 Program) of China (2010AA064905), the key discipline development project of CTBU (1252001), Changjiang Scholar Incentive Program (Ministry of Education, China, 2009), Natural Science Foundation of Chongqing (CSTC, 2010BB0260) and Project from Chongqing Education Commission (KJTD201020, KJZH11214, KJ090727).

References

[1] S. Mann, Self-assembly and transformation of hybrid nano-objects and nanostructures under equilibrium and non-equilibrium conditions, Nat. Mater. 8 (2009) 781–792.
[2] D.Q. Zhang, G.S. Li, J.C. Yu, Inorganic materials for photocatalytic water disinfection, J. Mater. Chem. 20 (2010) 4529–4536.
[3] C.Z. Wu, Y. Xie, Controlling phase and morphology of inorganic nanostructures originated from the internal crystal structure, Chem. Commun. (2009) 5943–5957.
[4] H.C. Zeng, Synthesis and self-assembly of complex hollow materials, J. Mater. Chem. 21 (2011) 7511–7526.
[5] X.W. Lou, L.A. Archer, Z.C. Yang, Hollow micro-/nanostructures: synthesis and applications, Adv. Mater. 20 (2008) 3987–4019.
[6] Y. Zhao, L. Jiang, Hollow micro/nanomaterials with multilevel interior structures, Adv. Mater. 21 (2009) 3621–3638.
[7] M.R. Jones, K.D. Osberg, R.J. Macfarlane, M.R. Langille, C.A. Mirkinl, Templated techniques for the synthesis and assembly of plasmonic nanostructures, Chem. Rev. 111 (2011) 3736–3827.
[8] J.G. Yu, H.T. Guo, S.A. Davis, S. Mann, Fabrication of hollow inorganic microspheres by chemically induced self-transformation, Adv. Funct. Mater. 16 (2006) 2035–2041.
[9] J. Zhang, F. Huang, Z. Lin, Progress of nanocrystalline growth kinetics based on oriented attachment, Nanoscale 2 (2010) 18–34.
[10] C.L. Wang, M.Y. Wang, K.P. Xie, Q. Wu, L. Sun, Z.Q. Lin, C.J. Lin, Room temperature one-step synthesis of microarrays of N-doped flower-like anatase TiO_2 composed of well-defined multilayer nanoflakes by Ti anodization, Nanotechnology 22 (2011) 305607.
[11] D.Y. Sung, I.Y. Kim, T.W. Kim, M.S. Song, S.J. Hwang, Room temperature synthesis routes to the 2D nanoplates and 1D nanowires/nanorods of manganese oxides with highly stable pseudocapacitance behaviors, J. Phys. Chem. C 115 (2011) 13171–13179.
[12] C.X. Lai, Q.B. Wu, J. Chen, L.S. Wen, S. Ren, Large-area aligned branched Cu_2S nanostructure arrays: room-temperature synthesis and growth mechanism, Nanotechnology 21 (2011) 215602.
[13] Y.F. Li, S.W. Tan, J.Y. Jiang, Z.Y. Huang, X.C. Tan, Room-temperature synthesis, growth mechanism and properties of uniform $CdMoO_4$ nano-octahedra, CrystEngComm. 13 (2011) 2649–2655.
[14] L.L. Wang, K.B. Tang, Z.P. Liu, D.K. Wang, J. Sheng, W. Cheng, Single-crystalline $ZnSn(OH)_6$ hollow cubes via self-templated synthesis at room temperature and their photocatalytic properties, J. Mater. Chem. 21 (2011) 4352–4357.
[15] P. Lianos, Production of electricity and hydrogen by photocatalytic degradation of organic wastes in a photoelectrochemical cell: the concept of the photofuelcell: a review of a re-emerging research field, J. Hazard. Mater. 184 (2011) 575–590.
[16] S. Rehman, R. Ullah, A.M. Butt, N.D. Gohar, Strategies of making TiO_2 and ZnO visible light active, J. Hazard. Mater. 170 (2009) 560–569.
[17] Z.H. Ai, L.L. Zhu, S.C. Lee, L.Z. Zhang, NO treated TiO_2 as an efficient visible light photocatalyst for NO removal, J. Hazard. Mater. 192 (2011) 361–367.
[18] F. Dong, S.C. Lee, Z.B. Wu, Y. Huang, M. Fu, W.K. Ho, S.C. Zou, B. Wang, Rose-like monodisperse mismuth subcarbonate hierarchical hollow microspheres: one-pot template-free fabrication and excellent visible light photocatalytic activity and photochemical stability for NO removal in indoor air, J. Hazard. Mater. 195 (2011) 346–354.
[19] R.D. Shannon, R.K. Waring, Synthesis and characterization of a new series of $BiOI_{1-x-y}Br_xCl_y$ pigments, J. Phys. Chem. Solid 46 (1985) 325–330.
[20] X. Zhang, Z.H. Ai, F.L. Jia, L.Z. Zhang, Generalized one-pot synthesis, characterization, and photocatalytic activity of hierarchical BiOX (X = Cl, Br, I) nanoplate microspheres, J. Phys. Chem. C 112 (2008) 747–753.
[21] Z.H. Ai, W.K. Ho, S.C. Lee, L.Z. Zhang, Efficient photocatalytic removal of NO in indoor air with hierarchical bismuth oxybromide nanoplate microspheres under visible light, Environ. Sci. Technol. 43 (2009) 4143–4150.
[22] Y.C. Feng, L. Li, J.W. Li, J.F. Wang, L. Liu, Synthesis of mesoporous BiOBr 3D microspheres and their photodecomposition for toluene, J. Hazard. Mater. 192 (2011) 538–544.
[23] J. Henle, P. Simon, A. Frenzel, S. Scholz, S. Kaskel, Nanosized BiOX (X = Cl, Br, I) particles synthesized in reverse microemulsions, Chem. Mater. 19 (2007) 366–373.
[24] J.X. Xia, S. Yin, H.M. Li, H. Xu, Y.S. Yan, Q. Zhang, Self-Assembly and enhanced photocatalytic properties of BiOI hollow microspheres via a reactable ionic liquid, Langmuir 27 (2011) 1200–1206.
[25] K. Zhang, J. Liang, S. Wang, J. Liu, K.X. Ren, X. Zheng, H. Luo, Y.J. Peng, X. Zou, X. Bo, J.H. Li, X.B. Yu, BiOCl sub-microcrystals induced by citric acid and their high photocatalytic activities, Cryst. Growth Des. 12 (2012) 793–803.
[26] C. Zhang, Y.F. Zhu, Synthesis of square Bi_2WO_6 nanoplates as high-activity visible-light-driven photocatalysts, Chem. Mater. 17 (2005) 3537–3545.
[27] M.S. Gui, W.D. Zhang, Preparation and modification of hierarchical nanostructured Bi_2WO_6 with high visible light-induced photocatalytic activity, Nanotechnology 22 (2011) 265601.
[28] F. Dong, W.K. Ho, S.C. Lee, Z.B. Wu, M. Fu, S.C. Zou, Y. Huang, Template-free fabrication and growth mechanism of uniform $(BiO)_2CO_3$ hierarchical hollow microspheres with outstanding photocatalytic activities under both UV and visible light irradiation, J. Mater. Chem. 21 (2011) 12428–12436.
[29] S. Shamaila, A.K.L. Sajjad, F. Chen, J.L. Zhang, WO_3/BiOCl, a novel heterojunction as visible light photocatalyst, J. Colloid Interface Sci. 356 (2011) 465–472.
[30] X. Chang, G. Yu, J. Huang, Z. Li, S. Zhu, P. Yu, C. Cheng, S. Deng, G. Ji, Enhancement of photocatalytic activity over $NaBiO_3$/BiOCl composite prepared by an in situ formation strategy, Catal. Today 153 (2010) 193–199.
[31] Y.Y. Liu, W.J. Son, J.B. Lu, B.B. Huang, Y. Dai, M.H. Whangbo, Composition dependence of the photocatalytic activities of $BiOCl_{1-x}Br_x$ solid solutions under visible light, Chem. Eur. J. 17 (2011) 9342–9349.
[32] W.D. Wang, F.Q. Huang, X.P. Lin, J.H. Yang, Visible-light-responsive photocatalysts xBiOBr−$(1-x)$BiOI, Catal. Commun. 9 (2008) 8–12.
[33] H.F. Cheng, B.B. Huang, Y. Dai, X.Y. Qin, X.Y. Zhang, One-Step synthesis of the nanostructured AgI/BiOI composites with highly enhanced visible-light photocatalytic performances, Langmuir 26 (2010) 6618–6624.
[34] X. Zhang, L.Z. Zhang, T.F. Xie, D.J. Wang, Low-temperature synthesis and high visible-light-Induced photocatalytic activity of BiOI/TiO_2 heterostructures, J. Phys. Chem. C 113 (2009) 7371–7378.
[35] T.B. Li, G. Chen, C. Zhou, Z.Y. Shen, R.C. Jin, J.X. Sun, New photocatalyst BiOCl/BiOI composites with highly enhanced visible light photocatalytic performances, Dalton Trans. 40 (2011) 6751–6758.
[36] H. Cheng, B. Huang, K. Yang, Z. Wang, X. Qin, X. Zhang, Y. Dai, Facile template-free synthesis of $Bi_2O_2CO_3$ hierarchical microflowers and their associated photocatalytic activity, ChemPhysChem. 11 (2010) 2167–2173.
[37] F. Dong, H.Q. Wang, Z.B. Wu, One-step green synthetic approach for mesoporous C-doped titanium dioxide with efficient visible light photocatalytic activity, J. Phys. Chem. C 113 (2009) 16717–16723.
[38] Y. Huang, Z.H. Ai, W.K. Ho, M.J. Chen, S.C. Lee, Ultrasonic spray pyrolysis synthesis of porous Bi_2WO_6 microspheres and their visible-light-induced photocatalytic removal of NO, J. Phys. Chem. C 114 (2010) 6342–6349.
[39] S.X. Ouyang, J.H. Ye, β-$AgAl_{1-x}Ga_xO_2$ solid-solution photocatalysts: continuous modulation of electronic structure toward high-performance visible-light photoactivity, J. Am. Chem. Soc. 133 (2011) 7757–7763.
[40] J.E.D. Davies, Solid state vibrational spectroscopy-the infrared and raman spectra of the Bismuth(III) oxide halides, J. Inorg. Nucl. Chem. 35 (1973) 1531–1534.
[41] X.X. Yu, J.G. Yu, B. Cheng, M. Jaroniec, Synthesis of hierarchical flower-like AlOOH and TiO_2/AlOOH superstructures and their enhanced photocatalytic properties, J. Phys. Chem. C 113 (2009) 17527–17535.
[42] W. Shao, F. Gu, L.L. Gai, C.Z. Li, Planar scattering from hierarchical anatase TiO_2 nanoplates with variable shells to improve light harvesting in dye-sensitized solar cells, Chem. Commun. 47 (2011) 5046–5048.
[43] J.G. Yu, Y.R. Su, B. Cheng, Template-free fabrication and enhanced photocatalytic activity of hierarchically macro/mesoporpous titania, Adv. Funct. Mater. 17 (2007) 1984–1990.
[44] K.S.W. Sing, D.H. Everett, R.A.W. Haul, L. Moscou, R.A. Pierotti, J. Rouquerol, T. Siemieniewska, Reporting physisorption data for gas/solid systems, Pure Appl. Chem. 57 (1985) 603–619.
[45] P.K. Surolia, R.J. Tayade, R.V. Jasra, Effect of Anions on the photocatalytic activity of Fe(III) salts impregnated TiO_2, Ind. Eng. Chem. Res. 46 (2007) 6196–6203.
[46] X.B. Chen, S.H. Shen, L.J. Guo, S.S. Mao, Semiconductor-based photocatalytic hydrogen generation, Chem. Rev. 110 (2010) 6503–6570.